Free Electron-Driven Photophysics in n-Type Doped Silicon Nanocrystals †

R. Limpens[a#] **& N.R. Neale**[a]

Abstract

Although there have been extensive speculations regarding the applicability of doped silicon nanocrystals (Si NCs) in optoelectronic technologies, a quantitative analysis on the photophysical workings of introduced free carriers remains elusive. Here, we present such a comprehensive study on the photophysics of ~7.5 nm heavily phosphorous-doped Si NCs, using a combination of spectroscopic techniques. We correlate the carrier dynamics with the location of the free carriers – which we tune from NC core to surface depending on the state of oxidation. The strength of the Coulomb interactions between the photoexcited electron-hole pairs and the doping-induced free carriers depends on (1) the concentration of free carriers, (2) the location of these carriers, and (3) the diameter of the NCs. In contrast to prior studies, the photoexcited carrier dynamics in these n-type doped Si NCs are dominated by strong Coulomb interactions with doping-induced free electrons, characterized by a negative trion lifetime of around 9 ns. While radiative recombination in doped direct bandgap NCs can often still compete with trion recombination (allowing emission to be present), emission in our doped Si NCs is completely quenched due to the relatively slow radiative recombination in these indirect bandgap NCs. Furthermore, multi-exciton interaction times are slightly shortened compared to those of intrinsic Si NCs, which we attribute to an increased number of free electrons, enhancing the oscillator strength of Auger recombination. These results constitute a framework for the optimization of doped Si NC synthesis techniques and device engineering directions for future doped-Si NC-based optoelectronic and photovoltaic applications.

Keywords: Silicon nanocrystals; phosphorus doping; coulomb interactions; ultrafast spectroscopy.

Introduction

Electronic doping of silicon nanocrystals (Si NCs) has stimulated several research fields in the last decade due to the possibility of visible-range plasmonic effects[1–3], increased electrical conductivities[4–7], tunability of the electronic structure[8] and alteration of the surface properties[9]. Doping of Si nanoparticles has even been executed to the extent at which simultaneous n- and p-type doping facilitates radiative recombination between donor-acceptor states[10]. This donor-acceptor co-doping enables efficient carrier multiplication[11] that is attractive for 3rd generation quantum dot solar cells[12]. Similar to what was previously observed for ensembles of intrinsic Si NCs[13,14]. As a result, the interest in highly doped nanostructures for (fast) carrier extraction devices, plasmonic applications[15] and e.g., fluorescent markers[16] is readily explained.

Despite these numerous advances in the field, only a handful of investigations have focused on the ultrafast carrier dynamics of these electronically complicated systems. In two recent publications, we addressed and confirmed the carrier multiplication potential of SiO_2-embedded phosphorous-boron (P-B) co-doped Si NCs by transient absorption spectroscopy[11,17] and reported on a surface passivation effect of the dopant atoms that reside at the Si NC surface/SiO_2 matrix interface in combination with impurity-induced trap states[17]. Furthermore, only one report discusses the ultrafast dynamics of colloidal dispersions of doped Si NCs (in this case B-doped)[18]. In this work, Diroll et al. observed optical switching potential of the transient absorption bleaching effect of the localized surface plasmon resonance (LSPR) mode, and derived sub-ps hole cooling times. Due to these rather limited efforts, an in-depth quantitative analysis on the electronic interaction between doping-induced free-carriers and photoexcited electron-hole (e-h) pairs in Si NCs remains elusive. This leads to seemingly contradicting studies on the absence/existence of photoluminescence (PL) in heavily doped Si NCs and the assumed strength of Coulomb-driven trion recombination[19–23].

In this work, we use multiple spectroscopic techniques to provide a comprehensive understanding of the carrier dynamics in relatively large (>7 nm) n-type P-doped Si NCs prepared via non-thermal plasma synthesis. The low impurity environment typical for this technique, and optimized in our laboratory, allows us to derive both the negative trion recombination rate and the biexciton recombination rate; two metrics that are driven by Coulomb interactions. These results quantify for the first time two of the most important nonradiative recombination channels in highly P-doped Si NCs.

Experimental

Sample production and functionalization

The P-doped Si NCs were produced by a modification of our previously reported non-thermal plasma method[24]. Briefly, 30 standard cubic centimeters per minute (sccm) of 10% silane (SiH_4) in helium, 30 sccm Ar, 3 sccm H_2, and 0.3, 0.5, or 0.7 sccm PH_3 gas flows were passed through a capacitively-coupled plasma at a pressure of 3.00 Torr in a 7.0 mm ID/9.5 mm OD quartz reactor tube. Forward RF power of 90 W was applied at 13.56 MHz using an Advanced Energy Cesar 136 generator through an Advanced Energy VM1000 matching network (tuned to give a reflected power of 0−1 W) to a copper ring electrode giving a delivered plasma power density of ~15 W cm^{-3}. A grounded electrode was positioned downstream and separated by ~1.5 cm from the working electrode. An Advanced Energy Z'Scan device was used to dynamically monitor the plasma conditions. NCs are created in the plasma through electron impact dissociation of SiH_4 and subsequent clustering of the fragments. Hydrogen-terminated Si NCs were collected downstream from the plasma on a 400-mesh stainless steel filter and transferred via load-lock to an inert-atmosphere argon-filled glovebox for collection. Samples were functionalized and purified similarly to our prior report[24], except radical initiation with ABCN was conducted at 140 °C for 3 h using neat 1-octadecene (dried over Na^0, distilled under N_2) rather than with 1-dodecene. The intrinsic Si NCs were produced following that same prior work[24].

Fourier-transform infrared (FTIR) spectroscopy

FTIR absorbance measurements were conducted on a Bruker Alpha FTIR spectrometer in transmission mode with a resolution of 4 cm−1. Gold coated Si plates were used for background measurements, and the NCs were drop-casted from toluene solutions on the substrates. Spectra were baseline-corrected using the concave rubberband correction method.

X-ray diffraction (XRD)

XRD measurements have been performed on a Rigaku D-max2500 diffractometer. The samples were drop-casted from a toluene solution on Si-based zero diffractions plates. To calculate the NC sizes from the XRD patterns we used the Scherrer-approach:

Eq3. $NC_{diameter} = \frac{k \cdot \lambda}{w \cdot \cos(c)}$,

With $NC_{diameter}$ the diameter of the NC, as shaping factor (k) we used 1.1[25], λ is the x-ray wavelength and w and c the width and center of the Si (111) diffraction peak. This modeling-procedure is verified by applying it on three differently sized intrinsic Si NC ensembles and comparing these results with structural analysis of other studies[24], as we show in the Electronic Supplementary Information (ESI, Figure S1). Moreover, a recent correlation of this XRD-approach with structural transmission electron microscopy (TEM) images confirms the robustness of this methodology as well[26].

Electron paramagnetic resonance (EPR)

EPR measurements were made using a high Q cavity on a Bruker E500, being equipped with a low background quartz crysostat. Scan parameters were adjusted as needed to avoid lineshape distortion and power saturation effects. We converted the applied magnetic field H (gauss), to the magnetic field independent g-value, following: hv=gβH, with h Planck's constant, v the cavity resonance frequency (Hz), g the g-value (unitless), β the Bohr magnetron (erg-sex/gauss).

Energy-dispersive X-ray spectroscopy (EDS)

EDS measurements were performed with a Si drift detector energy dispersive X-ray spectroscopy (EDS) system installed on a FEI ST30 Tecnai gun and was operated at 300 kV.

Time-resolved photoluminescence

Photoexcitation was conducted by using a Nd:YAG pumped optical parametric oscillator (OPO) (Spectra Physics Quanta Ray and GWU Premi Scan). Photoluminescence was detected in off-axis front-face geometry with a silicon avalanche photodiode (APD) (Thorlabs APD430A) attached to the other side, transducing transient optical signals with DC-400MHz bandwidth. A 650 longpass filter was used to block the excitation light (405 nm) and the signal from the APD was digitized using a fast oscilloscope (Tektronix DPO7254). We fit the trace with a stretched-exponential function, typical for ensembles of Si NCs[27]:

$$\text{Eq3.}\;\; I_{PL}(t) = I_0 \cdot \exp[-\left(\frac{t}{\tau}\right)^{\beta}] + y_0,$$

with $I_{PL}(t)$ the PL intensity at a specific time t, I_0 the PL intensity at t=0, τ the fitting lifetime, β the stretching component and y_0 representing the baseline specific to the experimental conditions. The TRPL data represents a stretching component β of 0.5, illustrating the significant broadening between the lifetime components[28]. This is expected since the experiment is conducted without a detection grating, and the TRPL trace therefore consists of contributions of multiple emission energies (i.e., different NC sizes and therefore different lifetimes) throughout the whole PL spectrum. The effective lifetime τ_{eff} is retrieved by uncoupling the dependent fitting parameters β and τ, according to the method of Guillos et al.[29].

Transient absorption (TA)

Ultrafast time-resolved measurements were collected by making use of a pump-probe technique with a femtosecond transient absorption spectrometer (Helios, Ultrafast Systems). As laser source we used a 4 W Ti-sapphire amplifier (Libra, Coherent), operating at 1 kHz and 100 fs pulse width. The fundamental beam (800 nm) was split, and a small portion (<5 mW) was used to create the near-infrared continuum (800–1700 nm). Another portion was attenuated with two neutral density filters and used as the excitation source after being modulated at 500 Hz. The time delay of the probe to the pump beam was varied with an exponential distribution between time delays of -2ps to 4 ns, with a 1s averaging at each delay point.

Results & discussion

Doping efficiency and formation mechanics

Effective substitutional P-doping of Si nanoparticles has been achieved by a variety of production methods such as co-sputtering[19], hydrogensilsesquioxane[30], plasma-enhanced chemical vapor deposition[6,21], ion implantation[23] and non-thermal plasma[2,31]. The non-thermal plasma approach could well be one of the most ideal synthesis techniques for P-doped NCs due to its close to 100% doping attachment/incorporation efficiency[32,33] and suppression of self-purification. This results from a combination of the relative low temperatures (~500 °C) and fast formation times (~ms)[32] typical for this method, leading to kinetic rather than thermodynamic control of dopant incorporation.

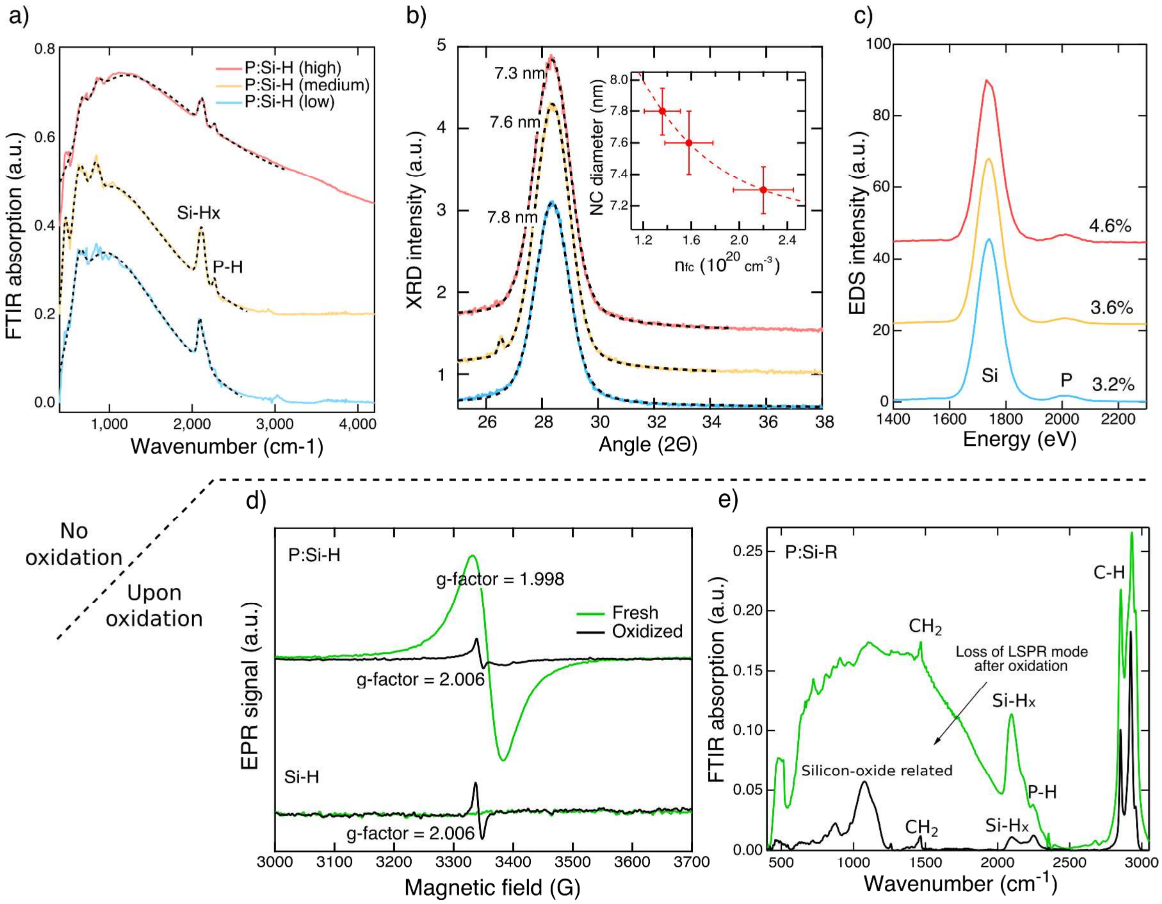

Figure 1. Structural characterization of un-oxidized (a-c) and oxidized (d-e) P:Si–H . a) FTIR spectra of all three P-concentrations. Log-normal fits of the LSPR modes are represented by the black dashed lines. b) Main panel: XRD patterns of all three P-concentrations. The dashed line is a Voight fit. Inset: NC diameter (from XRD) as a function of the free carrier concentration, n_{fc} (from FTIR). The red dashed line represents an exponential fit and functions as a guide to the eye. The error bars represent the fitting errors. c) EDS spectra in which the integrated ratios display the elemental composition. d) EPR measurements as a function of the applied magnetic field, before (green) and after complete oxidation of one week (black) for Si–H and P:Si–H. e) FTIR spectra of (functionalized) medium doped P:Si-R, before (green) and after (black) oxidation.

We produced P-doped Si NCs through the nonthermal plasma synthesis method and vary doping concentrations by changing the PH_3 content relative to SiH_4. Figure 1a-d presents data on the as-produced NC powder with H-passivated surfaces – hereafter referred to as P:Si–H. Figure 1a shows diffuse reflectance Fourier transform infrared (referred to simply as FTIR) spectra of the systems. The Si–H_x stretching modes of the surface *SiH_x groups (where the asterisk denotes a surface atom) are visible around 2100 cm^{-1},[24] and P–H stretching modes originating from surface *PH_x groups appear at 2276 cm^{-1}. Notably, these surface *PH_x groups do not contribute to doping since they are electronically satisfied (octet rule); only substitutional dopant sites (P for Si) result in electronic doping. In addition, the FTIR data show a clear localized surface plasmon resonance (LSPR) mode – reflecting a collective oscillation of free carriers – for all three samples, represented by the broad log-normal shaped absorption feature peaking around ~1000 cm^{-1}. We calculate the free carrier concentration (n_{fc}) from the LSPR peak following Ref.[26] and find the number of free carriers per NC of 34, 36, and 45 for 7.8, 7.6, and 7.3 nm diameter samples, respectively (Table 1 and associated analysis in ESI). For detailed modelling procedures of the LSPR feature in Si NCs we direct the interested reader to Refs.[34–36]. The diameters (D_{NC}) are retrieved by applying a Scherrer analysis[37] on the X-ray diffraction (XRD) patterns of Figure 1b (Methods). Slight reduction in the NC diameter with increasing doping density (inset of Figure 1b) is most likely the result of the impedance of Si cluster coagulation (the process by which larger spherical particles are formed)[32] by *PH_x groups. By using geometrical arguments, we estimate the number of Si atoms in a certain sized NC and calculate an effective substitutional doping fraction (D_{subst}) of 0.27, 0.32 and 0.44 at. %, respectively. These D_{subst} values are ~1 order of magnitude less than the total atomic percentage of P atoms (T_{Patoms}) – quantified from an integrated energy dispersive X-ray spectroscopy (EDS) analysis, Figure 1c – that ranges from 3.2–4.6 at. % with increasing P-concentrations. We thus achieved a doping efficiency (D_{eff}) of ~10%, in line with existing literature for the non-thermal plasma synthesis method[31,33].

D_{NC} [nm]	n_{fc} [10^{20}cm^{-3}]	#fc/NC	D_{subst} [at. %]	T_{Patoms} [at. %]	D_{eff} [%]
7.8	1.36	34	0.27	3.2	8.4
7.6	1.58	36	0.32	3.6	8.9
7.3	2.20	45	0.44	4.6	9.6

Table 1. Sample details of the non-thermal plasma produced P-doped Si NCs.

Figure 1d displays electron paramagnetic resonance (EPR) spectra both before and after oxidation of P:Si–H and intrinsic Si NCs (Si–H). The Si-H were produced by the same technique and serve as reference measurement. The pre-oxidized EPR measurements of both the Si–H and P:Si–H confirm the high quality samples from our production technique, as opposed to the defect-related signal resulting from dangling bonds previously observed in other Si NC systems[2,38–40]. This absence of a dangling bond-related feature also tells us that the calculated n_{fc} can be rightfully used to calculate the percentage of substitutional doping sites (D_{subst})[26], as we did in Table 1. Moreover, the un-oxidized P:Si–H show a strong feature at a g-factor=1.998, as expected from substitutional P-doping in a crystalline Si lattice[7,41]. Upon the introduction of oxygen, a broad EPR-signal centered around a g-factor of ~2.006 arises for both samples, indicative of free radicals in an immobilized environment (i.e., dangling bonds)[7,39]. Removal of the ~1.998 free-electron feature for the P:Si–H goes hand in hand with the upcoming surface oxidation. This is consistent with the recent work of Kortshagen et al.[2], who assigned it to the tunneling of free carriers from the Fermi level of the NC core to the surface-adsorbed oxygen: the so-called Cabrera-Mott theory[42].

The rest of this work focusses on the samples in colloidal form. This allows us to focus solely on the photophysics of free-standing NCs, reduce scattering effects and control the optical density of our samples. Similar to our prior reports,[24,43] Si NC dispersions were prepared using a thermally-initiated reaction between octadecene and as-prepared, hydride-terminated Si NCs to functionalize the NC surfaces with long-chain alkyl ligands, denoted as P:Si–R (Methods). The exact functionalization mechanism is discussed in detail in Ref.[24]. Figure 1e presents the FTIR spectra of the P:Si–R (medium doped) and shows that the ligand functionalization process does not significantly affect the carriers within the Si NC lattice. In addition to the LSPR feature, C–H vibration modes from the hydrocarbon ligands (~1490 and ~3000 cm^{-1}) and minor silicon oxide features ~1070 cm^{-1} are observed following functionalization. Trace oxidation appears to be unavoidable in our functionalized samples as well as those throughout literature[24,44–46], and further on we will discuss its impact on the carrier dynamics. Upon intentional oxidation by air exposure, the Si–O stretching features become much more prominent and the LSPR mode vanishes, indicating that the minimal amount of free carriers necessary to support a plasmon mode (>10)[1] is no longer present, in line with the before-mentioned Cabrera-Mott theory[42]. Time-dependent FTIR-measurements indicating the oxidation rate, i.e., the loss of the LSPR mode, are given in Figure S2. In addition, we present consistent EPR and XRD measurements on the ligated NC systems in Figure S3 and S4, respectively.

Photoluminescence from heavily n-type doped NCs

We next focus on the photoexcited carrier dynamics by two mutually connected approaches: PL and ultrafast transient absorption spectroscopy. It is somewhat surprising that PL has been observed in several P-doped NC systems[19,20,22,23] due to the fast ~ps nature of typical Auger interactions that dominate the photophysics in these systems[47,48]. The observation of emission in these systems could indicate that negative trion recombination is unexpectedly weak, enabling radiative recombination on the μs-timescale to successfully compete with trion recombination. In recent work we showed this is indeed the case for small diameter doped Si NCs (D_{NC}<6 nm), in which the interaction of dopant-induced carriers with photo-excited e-h pairs is negligible small due to the large binding energies of carriers in strongly quantum-confined systems[17]. For larger NCs, as studied in this report, such a scenario seems unlikely. In this case, PL most probably arises from a non-doped subset of the NC ensemble. This can arise because of the statistical nature of the doping mechanism as described by Kroupa et al. for Ag-doped PbSe NCs[49], or the oxidation-induced free carrier extraction from the core (further on referred to as oxide-compensated NCs) as we described above.

In our system, the effect of oxide-compensated NCs on the PL is clearly observed based on the time-resolved emission spectra in Figure 2a. Directly upon functionalization, a weak PL spectrum is detected or the medium doped P:Si–R which grows in upon purposefully opening up the cuvette to ambient air, i.e., oxygen, being accompanied by a small red shift (with the PL peak moving from ~880 to ~920 nm) – inset Figure 2a. From Figure S2 we note that the NC sizes remain unchanged upon oxidation. The fact that the Si NC size does not change yet the PL peak energy red-shifts over time suggests that the subset of effectively undoped NCs changes over oxidation time. This is explained by the fact that larger NCs – consisting of more atoms than small NCs – are on average doped with a higher number of dopants at a certain free carrier concentration. As such, the emission at early times (hours) is dominated by the smallest NCs which reach the oxygen-compensated state faster due to their smaller free carrier concentration. Over time, additional oxidation fully extracts the charges from larger NCs as well that then contribute to, and red-shift the, ensemble PL spectrum.

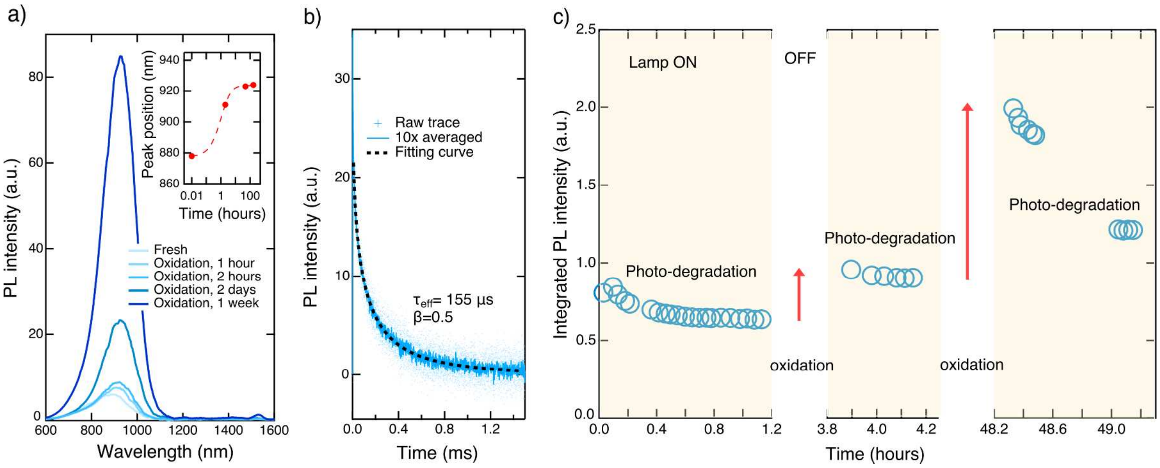

Figure 2. PL spectra and dynamics of functionalized medium P-doped Si NCs (P:Si-R). a) Main panel: PL spectra for increasing oxidation times (i.e. with increasing darkening of the blue color-coding). Excitation has been performed by a 405 nm LED. Inset: Peak position as a function of oxidation time, as derived from a Gaussian fitting procedure. The red dashed line is a Lorentzian fit and serves as a guide to the eye. b) Time-resolved PL measurements of the 1-week oxidized nanoparticles. The light blue trace represents the raw data, the darker blue trace is a 10x average of the original dataset, and the black dashed line is a stretched exponential fitting model, defining the average effective lifetime to be 155 µs. c) Integrated PL intensities (from panel a) as a function of time. The yellow parts indicate a situation of continuous illumination of the nanoparticles (ON-times). The white (axis-less) parts represent time-intervals of non-illumination (OFF-times).

The stretched exponential shape and decay rate of the time-resolved PL measurements (Figure 2b) confirm the excitonic origin of the radiative recombination feature (experimental conditions and fitting procedure are presented in the Methods). We find an effective lifetime of τ_{eff} =155 µs, in line with previously reported rates for similar-sized Si NCs[50,51]. In Figure 2c we monitor the PL intensity dependence upon illumination, and upon oxidation, in more detail. The "Lamp ON" state refers to a continuous CW 405 LED excitation, whereas the shutter is closed for the "LAMP OFF" situation. Upon illumination, the brightness of the PL decreases in time, which is commonly observed in quantum-confined materials and often related to charging of the nanoparticles upon photo-excitation. This is explained by electron/hole transfer to a trap state that charges the NC core by leaving the hole/electron behind in the conduction/valence band, invoking efficient trion recombination in the NC core[52,53]. After a time-interval of non-illumination (illustrated by the gap between time domains) the surface oxygen-induced PL takes over completely, and the intensity surpasses the original magnitude of before the photo-charging effect.

Trion-dominated ultrafast carrier dynamics in the single exciton regime

Transient absorption measurements were further used to quantify the Auger interactions that lie at the origin of the observed PL features. The measurements have been executed in the single-exciton excitation regime[47]. The experiments were conducted with a pump and probe wavelength of λ_{pump} = 500 nm and λ_{probe} = 1100–1250 nm, respectively. We therefore probe photoexcited e-h pairs by making use of strong intraband absorptions, typical for Si NCs[13,54], and hereby preclude potential lattice heating effects from appearing in the traces, as observed by Ref.[18]. Due to the intraband nature of our experiment we further on use the term induced absorption (IA). The main panel of Figure 3a compares the ultrafast carrier dynamics of the P:Si–R at the three doping concentrations. The traces can be well fitted with a double exponential decay function. We make two main observations. First, for all samples, a strong reduction of the carrier signal appears on a short (~6 ps) timescale. Such a fast signal decrease is often observed for intrinsic Si NC ensembles and several models have been employed to explain this behavior such as hot-carrier relaxation[55] and trap-state induced recombination[47,56]. However, our fast component is independent of the pump energy used (with the pump energy ranging from 400–600 nm, as shown in Figure S3), excluding the hot carrier relaxation effect. The fast component is therefore in line with the formation of some surface defects upon functionalization (which we will confirm upon discussing Figure 3c). This is most likely due to the trace oxidation observed in the FTIR spectra of Figure 1e. Hence, a significant fraction of the carriers (based on our traces we assume ~10-30%) are lost as a result of these defects within the first couple of ps. This illustrates the difficulty of producing ultrahigh emission efficiencies in Si NCs, as indicated by several studies[40,57,58]. We thus observe two opposite effects upon oxidation that both involve dangling bonds at the surface. (i) oxide-compensation (Figure 2) that increases the optical activity and (ii) dangling bond-initiated ultrafast non-radiative quenching. Our second main observation is a strong nonradiative recombination channel in the sub-ns regime (~250 ps) that shortens as a function of the doping concentration (inset of Figure 3a), in line with the Coulomb-driven Auger interactions between the free carriers and photoexcited e-h pairs. We argue that, in contrast to multi-exciton interactions, which follow an n_{eh}^2 or n_{eh}^3 behavior depending on the interaction model[47] (with n_{eh} being the number of e-h pairs), trion interactions should just simply depend on n, with n representing the number of free carriers, following:

$$\text{Eq1. } \tau_{A,X-} = \tau_{A,X-_n} \cdot n,$$

with $\tau_{A,X-}$ the negative trion lifetime, $\tau_{A,X-n}$ the lifetime of an e-h pair in the vicinity of n number of free electrons (i.e., the Auger component in the inset of Figure 3a). The negative trion lifetime is calculated for all samples using Eq.1 and we find a lifetime of $\tau_{A,X-}$ 10.5, 8.7 and 8.5 ns with decreasing NC size. These negative trion lifetimes are ~4-5 orders of magnitude faster than the excitonic band-to-band radiative recombination, hereby preventing any possibility of radiative recombination from n-type doped NCs. This is in contrast to doped versions of direct bandgap NCs[59–61] in which efficient radiative recombination will compete with Coulomb-driven Auger interactions.

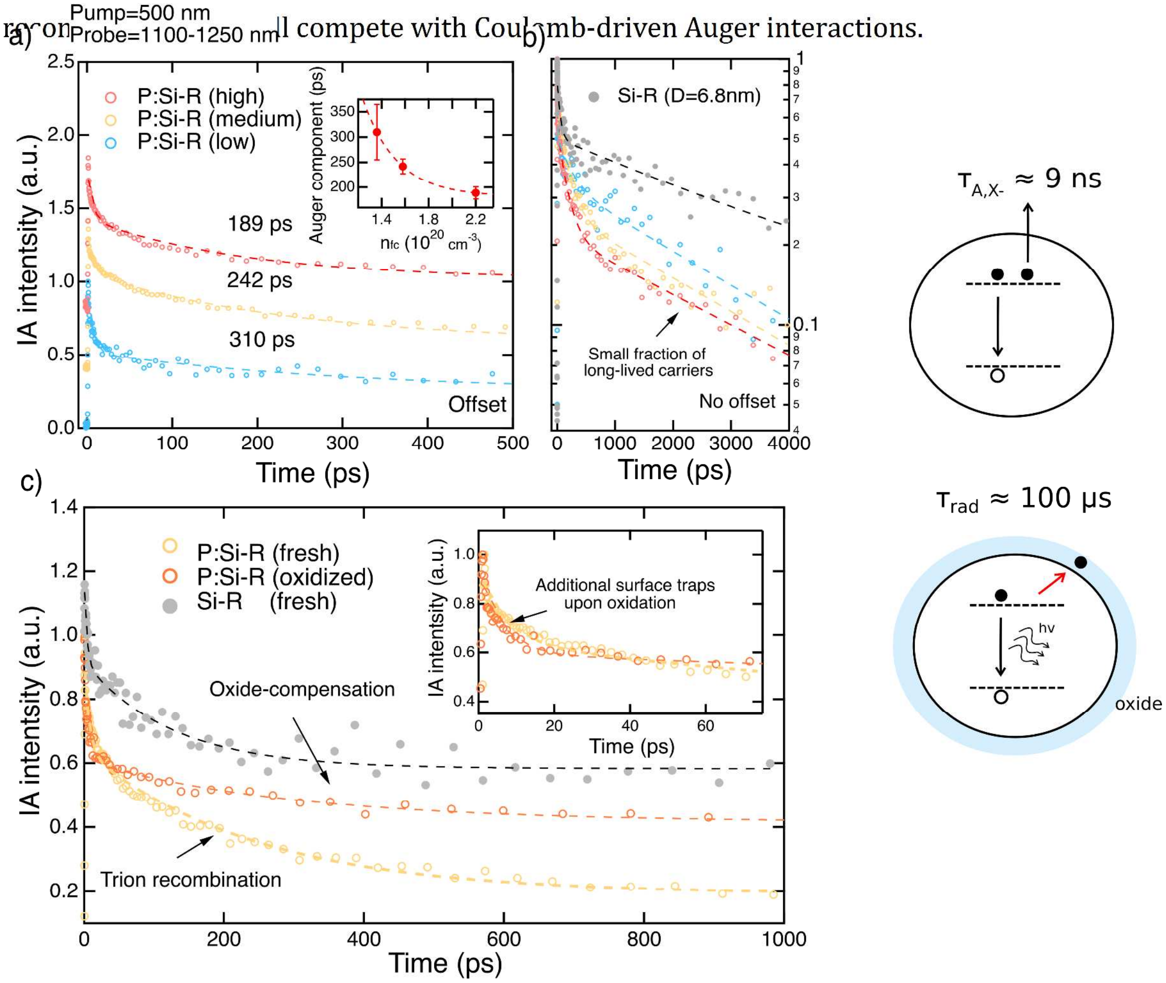

Figure 3. a) Main figure: Dynamics of the P:Si-R for the different doping concentrations, within the first 500 ps after photo-excitation. The traces are presented with an offset. The dashed lines represent double exponential decays, consisting of a fast (~6 ps) process, followed by a nonradiative Auger recombination channel of ~250 ps. Inset: Recombination rate of the Auger decay component as a function of the free carrier concentration, n_{fc}. b) Dynamics

at longer time-scales (Δt<4 ns). The grey disks represent a typical trace for an ensemble of intrinsic Si NCs (D_{NC}=6.8 nm). No offset has been used for these long time-scale traces. All traces are normalized to 1 at their maximum IA intensity. The dashed lines function as guides to the eye. c) IA traces of the medium doped P:Si-R before oxidation (yellow dots) and after one week of oxidation (orange dots). Main panel: Traces with a time-delay up to 1 ns. For comparison, we inserted the same intrinsic Si NC trace (grey disks) as in panel (b). The dashed lines function as guides to the eye. Inset: short time-scale comparison of the fresh and oxidized P:Si–R. The scheme on the right side depicts the trion interaction model as discussed in the main text.

The analysis above illustrates that within 4 ns of photo-excitation of the P:Si–R Si NCs nearly all photoexcited *e-h* pairs have recombined nonradiatively. The PL observed in Figure 2 however originates from a small fraction of e-h pairs that populate a long-lived state in the aforementioned effectively undoped NCs (these can be undoped due to the statistical doping argument and/or oxide-compensation). This is consistent with the IA traces in Figure 3b, which demonstrate that the magnitude of this long-lived fraction decreases with increasing doping concentration. The higher the doping concentration, the more difficult it is to sweep out all free carriers via the Cabrera-Mott process. For comparison, a trace of intrinsic Si–R NCs is displayed in Figure 3b as well, showing a larger fraction of long-lived e-h pairs, in line with the much higher optical activities for intrinsic Si NCs, as reported in several reports[20,22,58].

Furthermore, to directly relate the oxidation-induced PL features from Figure 2 with the ultrafast carrier dynamics we compare IA measurements for the medium doped P:Si–R in an un-oxidized (yellow markers) and oxidized state (orange) in Figure 3c. Note that the EPR measurements (Figure 1d) already indicated that oxidation introduced dangling bonds on the surfaces of the –H terminated NCs. Figure 3c now shows that the ~6 ps surface defect-related recombination channel is enhanced for the oxidized P:Si–R. We thus relate this to the introduction of dangling bonds upon oxidation. Furthermore, these data directly probe the oxygen-compensation effect: the data of the oxidized P:Si–R NCs mimics that of the intrinsic NCs (grey disks), confirming the absence of free carriers in the oxidized sample.

A scheme of the photophysical model with the belonging quantification of the time-scales is presented on the right side of Figure 3. Hence, both by changing the doping concentration in the production phase and post-production (by oxidation), we were able to alter the carrier dynamics in the ps time-regime. Note that the oxygen-compensated experiments (Figure 2 and 3c) are essential in light of this study. They allow us to safely assign the observed ~ 250 ps carrier quench for the unoxidized NCs (Figure 3a) to negative trion recombination. The only possible alternative scenario for this quench would be that P-doping deforms the crystalline structure and introduces defect states. The number of these defect states could also increase with the doping concentration, explaining the shortened lifetimes with the doping concentration in the inset of Figure 3a just as well. The oxygen-compensation does however solely interact with the free carriers without changing structural defects in the NC core. Still we observe upcoming PL (Figure 2) and a neutralization of the ~250 ps carrier quench (Figure 3c). We can therefore eliminate the defect-argument as a potential explanation of our results.

Multi-exciton interactions in the multi-exciton excitation regime

Next, we study the multi-exciton interactions in the P:Si–R by increasing the pump fluence to generate multiple e-h pairs within each NC. We expect that the rate of multi-exciton interactions will increase in doped relatively to intrinsic samples since the oscillator strength of Auger recombination should increase upon the introduction of additional initial states (the free electrons). The main panel of Figure 4a displays IA traces of the medium doped P:Si–R at several excitation fluences. As a result of Auger recombination between multiple e-h pairs in the same NC, a fastening of the carrier dynamics in the initial hundreds of picoseconds is observed for high excitation intensities (> 100 nJ, Figure 4a inset). The biexciton lifetime is extracted according to the approach of Klimov[62]. This is performed by (1) normalizing the multi-exciton-dominated trace to point B. Subsequently, (2) the single-exciton regime trace is subtracted from the multi-exciton trace to arrive at the “scaled nonlinear trace” as referred to on the y-axis of Figure 4b. This method allows separating the biexciton recombination from higher order multi-exciton recombination pathways by simply picking out the exponential decay components. In the excitation regime used here, these higher order interactions consist mainly of the triple-exciton recombination feature, which is reflected by the decay component in the initial tens of picoseconds. Hence, a double exponential fit is used to fit the scaled non-linear trace in which the longer component represents the bi-exponential decay time.

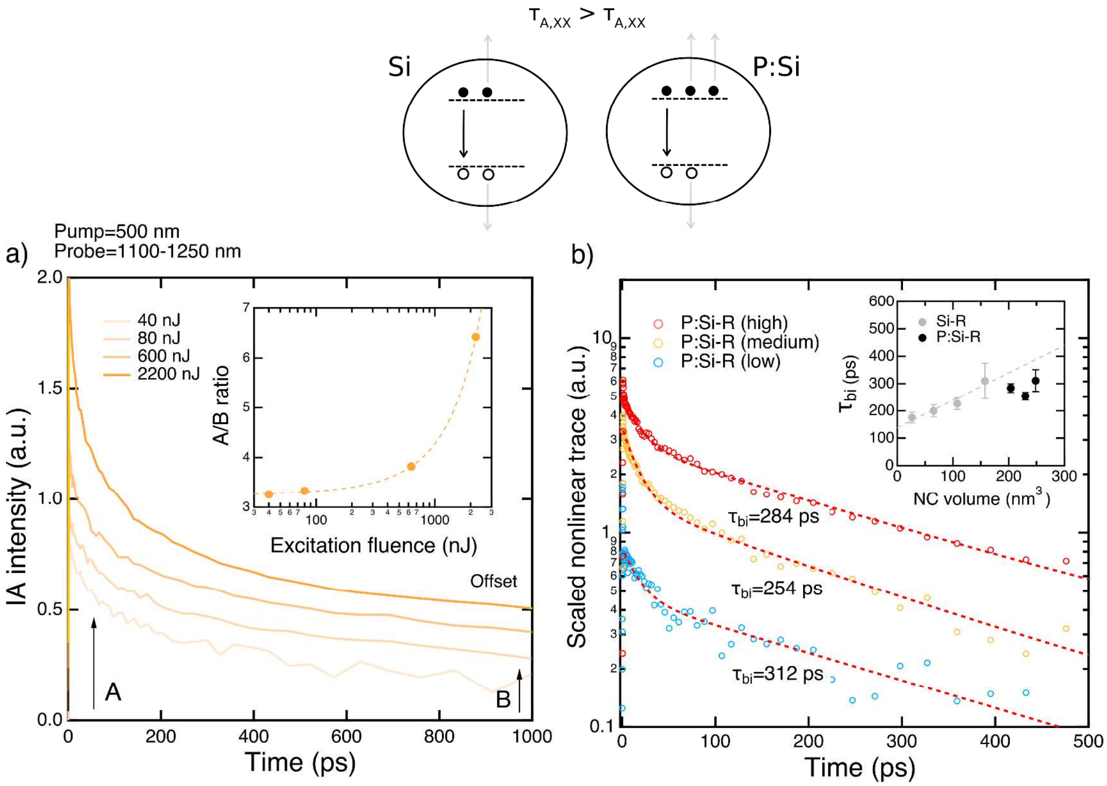

Figure 4. Multi-exciton interactions of the functionalized P-doped NCs (P:Si-R). a) Main panel: IA traces of the medium doped P:Si–R , for several excitation intensities. The traces have been normalized to the intensity at 1 ns (point B) and an offset is applied for clarity. Inset: A/B ratios, with A the magnitude at 1 ps, as a function of the excitation fluence. An excitation spot of 1mm in diameter has been used. The orange dashed line is a polynomial fit and functions as a guide to the eye. b) Main panel: Log-lin plot of the scaled nonlinear IA traces, according to the method of Klimov.[62]*, for all three P concentrations. All traces represent a double exponential decay (the fits are displayed by the red dotted lines). Inset: biexciton lifetime as a function of the NC volume for the P:Si–R (black dots) and intrinsic Si NCs (gray dots). The linear fit (gray dashed line) represents the universal* r^3 *dependence of the biexciton lifetime. The error bars represent the fitting errors. The scheme on top depicts the biexciton interaction.*

The inset of figure 4b presents the derived biexciton lifetimes as a function of the NC volume. Auger interactions typically follow universal r^3 dependencies, both for direct and indirect semiconductor nanocrystals[63]. For intrinsic Si–R this r^3 relationship is upheld as shown by the biexciton lifetimes for samples ranging from 3.7-6.7 nm in diameter (gray dots in the inset of Figure 4b). These Si–R samples were purposefully prepared to serve as a reference for this study. The experimental derivation of these values is presented in Figure S4. However, the P:Si–R NCs seem to break this rule in comparison to their intrinsic cousins. The biexciton lifetime of these doped NCs (black dots in the inset of Figure 4b) is fastened with a factor ~ 0.8 compared to the extrapolation of the r^3 dependence of the intrinsic NCs (gray dashed line). Although the P:Si–R samples consists of different doping concentrations, this trend is valid for all three samples and we explain this by the additional electrons that increase the oscillator strength of Auger recombination upon P-doping. Note that the difference is relatively small (only a factor ~0.8), especially considering the significant amount (>30) of free carriers present. As a possible explanation we mention that the incorporation of P-atoms in the Si lattice could lower the density of states in the conduction band[64], hereby actually decreasing the strength of the Auger interaction upon doping. Furthermore, we also are aware of the lighter effective mass of the electron (m_e0.26) compared to the hole (m_h0.4) that creates hole-dominated Auger recombination. Additional electrons should therefore have a relative small effect on the overall strength of the interaction.

In addition, we tried to model the Auger interactions of the P:Si–R NCs using a stochastic modeling approach, as previously used by us to model the multi-exciton excitation regime of solid state dispersions of P-B co-doped Si NC ensembles[17]. As shown in Figure S5, it was however not possible to fit the data using either a three-charge interaction model or an exciton interaction model[47]. The inability of fitting the multi-exciton dynamics with a standard interaction model is another indication of the influence of the free carriers on the biexciton Auger interactions and shows conclusively that such interactions cannot be treated by a symmetric approach.

Finally, it is worthwhile to compare our results to the extensive work of Park et al.[60], who proposed a universal dependence describing the biexciton Auger decay as a superposition of uncorrelated negative and positive trion pathways:

$$\text{Eq2. } \frac{1}{\tau_{A,XX}} = 2\left(\frac{1}{\tau_{A,X-}} + \frac{1}{\tau_{A,X+}}\right),$$

with $\tau_{A,XX}$ the biexciton lifetime, $\tau_{A,X-}$ and $\tau_{A,X+}$ the negative and positive trion lifetime, respectively. Upon assuming similar electron and hole effective masses ($\tau_{A,X-} = \tau_{A,X+}$), Park et al. proposed that the correlation can be rewritten as $4\tau_{A,XX} = \tau_{A,X-} = \tau_{A,X+}$. In this study, we derived both quantities ($\tau_{A,XX} \cong 280$ ps and $\tau_{A,X-} \cong 9$ ns) and report on a difference of a factor ~30, in contrast to the factor 4 described by Park et al. We believe that the factor of ~30 found here more accurately describes the biexciton Auger decay in Si NCs since our analysis accounts for effective mass differences between electrons and holes, which will influence the density of states and the localization of the wave functions, hereby leading to $\tau_{A,X-}$ that could be significantly longer than $\tau_{A,X+}$. Such a large difference between the negative and positive trion lifetimes in Si NCs is consistent with that observed for CdSe[61], CdSe/ZnSe[65] and CdSe/CdS[66] quantum dots.

Conclusions

In conclusion, making use of a non-thermal plasma synthesis method and a variety of spectroscopic investigations we provide a quantitative analysis of the carrier dynamics in P-doped Si NCs. The strength of the Coulomb interactions between the photoexcited electron-hole pairs and the doping-induced free carriers depends on (1) the concentration of free carriers, (2) the location of these carriers – residing in the NC core or at the surface – and (3) the diameter of the NC. Coulomb-driven Auger recombination dominates the carrier dynamics in >7 nm P-doped Si NCs, with a negative trion lifetime of $\tau_{A,X-} \cong 9$ ns. Moreover, we observe a small perturbation of the biexciton lifetime in comparison to that of intrinsic Si NCs and ascribe this to the increased number of initial states due to the presence of a significant number of free electrons. Although we show that Auger-induced trion recombination prevails over radiative recombination in these highly n-type doped indirect semiconductor nanostructures, we do observe PL. This is explained by free electron diffusion to the oxidized surface, effectively cleaning the NC core from free electrons and suppressing their forthcoming Coulomb interactions with the photoexcited e-h pairs. These results provide insight into some of the conflicting reports regarding the strength of Coulomb interactions in doped Si NCs. This combined with the quantification of both the negative trion and biexciton recombination rate, should provide a comprehensive basis for future Si NC-based optoelectronic and photovoltaic applications dealing with doped NCs.

Conflict of interest

There are no conflicts to declare.

Acknowledgements

R.L. acknowledges the National Renewable Energy Laboratory (NREL) LDRD program for the award of the Nozik post-doctoral Fellowship to perform this research. N.R.N. was supported by the U.S. Department of Energy, Office of Science, Office of Basic Energy

Sciences, Division of Chemical Sciences, Geosciences, and Biosciences, Solar Photochemistry Program under contract number DE-AC36-08GO28308 to NREL. The authors thank Noah Bronstein for his help with the EDS characterization, Gerard M. Carroll and Gregory Pach for their help with the sample preparation in addition to David Mulder and David Bobela for their EPR expertise.

Footnotes

[a] National Renewable Energy Laboratory, 15013 Denver West Parkway, Golden, CO 80401, USA.

#Corresponding author: Rens Limpens: rens.limpens@nrel.gov

†Electronic supplementary information (ESI) available. See DOI:

TOC-figure

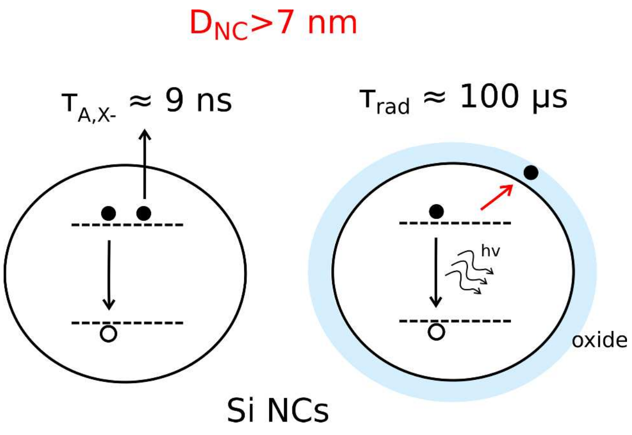

By making use of multiple spectroscopic techniques we provide a comprehensive understanding of the photophysics of n-type doped Si nanocrystals.

References

1 J. M. Luther, P. K. Jain, T. Ewers and A. P. Alivisatos, *Nat. Mater.*, 2011, **10**, 361–366.

2 N. J. Kramer, K. S. Schramke and U. R. Kortshagen, *Nano Lett.*, 2015, **15**, 5597–5603.

3 K. Kneipp, Y. Wang, H. Kneipp, L. T. Perelman and I. Itzkan, *Phys. Rev. Lett.* 1997, **78**, 1667–1670.

4 D. Shan, Y. Ji, D. Li, J. Xu, M. Qian, L. Xu and K. Chen, *Appl. Surf. Sci.*, 2017, **425**, 492–496.

5 T. Chen, K. V. Reich, N. J. Kramer, H. Fu, U. R. Kortshagen and B. I. Shklovskii, *Nat. Mater.*, 2016, **15**, 299–303.

6 D. Shan, M. Qian, Y. Ji, X. Jiang, J. Xu and K. Chen, *Nanomaterials*, **6**, 233.

7 A. R. Stegner, R. N. Pereira, K. Klein, R. Lechner, R. Dietmueller, M. S. Brandt, M. Stutzmann and H. Wiggers, *Phys. Rev. Lett.*, 2008, **100**, 18–21.

8 Y. Hori, S. Kano, H. Sugimoto, K. Imakita and M. Fujii, *Nano Lett.*, 2016, **16**, 2615–2620.

9 S. Zhou, Z. Ni, Y. Ding, M. Sugaya, X. Pi and T. Nozaki, *ACS Photonics*, **3**, 415-422.

10 H. Sugimoto, M. Fujii, K. Imakita, S. Hayashi and K. Akamatsu, *J. Phys. Chem. C*, 2013, **117**, 11850–11857.

11 N. Xuan Chung, R. Limpens, C. de Weerd, A. Lesage, M. Fujii and T. Gregorkiewicz, *ACS Photonics 2018 (just accepted)*.

12 F. Priolo, T. Gregorkiewicz, M. Galli and T. F. Krauss, *Nat. Nanotechnol.*, 2014, **9**, 19–32.

13 M. T. Trinh, R. Limpens, W. D. A. M. De Boer, J. M. Schins, L. D. A. Siebbeles and T. Gregorkiewicz, *Nat. Photonics*, 2012, **6**, 316–321.

14 B. Bruhn, R. Limpens, N. X. Chung, P. Schall and T. Gregorkiewicz, Sci. Rep. 2016, **6**, 20538.

15 Z. Ni, L. Ma, S. Du, Y. Xu, M. Yuan, H. Fang, Z. Wang, M. Xu, D. Li, J. Yang, W. Hu, X. Pi and D. Yang, *ACS Nano*, 2017, **11**, 9854–9862.

16 P. Das and N. R. Jana, *ACS Appl. Mater. Interfaces*, 2014, **6**, 4301–4309.

17 R. Limpens, M. Fujii, N. R. Neale and T. Gregorkiewicz, *J. Phys. Chem. C.,* 2018, **122**, 6397-6404*.*

18 B. T. Diroll, K. S. Schramke, P. Guo, U. R. Kortshagen and R. D. Schaller, *Nano Lett.*, 2017, **17**, 6409–6414.

19 A. Mimura, M. Fujii, S. Hayashi, D. Kovalev and F. Koch, *Phys. Rev. B.*, 2000, **62**, 12625–12627.

20 P. Lu, W. Mu, J. Xu, X. Zhang, W. Zhang, W. Li, L. Xu and K. Chen, *Sci. Rep.*, 2016, **6**, 1–12.

21 D. Hiller, J. López-Vidrier, S. Gutsch, M. Zacharias, K. Nomoto and D. König, *Sci. Rep.*, 2017, **7**, 1–12.

22 D. Li, Y. Jiang, J. Liu, P. Zhang, J. Xu, W. Li and K. Chen, *Nanotechnology*, , DOI:10.1088/1361-6528/aa852e.

23 M. Frégnaux, R. Khelifi, D. Muller and D. Mathiot, *J. Appl. Phys.*, 2014, **116**, 143505.

24 L. M. Wheeler, N. C. Anderson, P. K. B. Palomaki, J. L. Blackburn, J. C. Johnson and N. R. Neale, *Chem. Mater.*, 2015, **27**, 6869–6878.

25 A. L. Patterson, *Phys. Rev.*, 1939, **56**, 978–982.

26 D. J. Rowe, J. S. Jeong, K. A. Mkhoyan and U. R. Kortshagen, *Nano Lett.*, 2013, 13, 1317-1322.

27 R. Limpens, A. Lesage, P. Stallinga, A. N. Poddubny, M. Fujii and T. Gregorkiewicz, *J. Phys. Chem. C*, 2015, **119**, 19565–19570.

28 F. Sangghaleh, I. Sychugov, Z. Yang, J. G. C. Veinot and J. Linnros, *ACS Nano*, 2015, **9**, 7097–7104.

29 O. Guillois, N. Herlin-Boime, C. Reynaud, G. Ledoux and F. Huisken, *J. Appl. Phys.*, 2004, **95**, 3677–3682.

30 H. Sugimoto, M. Fujii and K. Imakita, *Nanoscale,* 2014, **6**, 12354-12359.

31 X. D. Pi, R. Gresback, R. W. Liptak, S. A. Campbell and U. Kortshagen, *Appl. Phys. Lett.*, 2008, 92, 123102.

32 U. R. Kortshagen, R. M. Sankaran, R. N. Pereira, S. L. Girshick, J. J. Wu and E. S. Aydil, *Chem. Rev.*, 2016, **116**, 11061–11127.

33 A. R. Stegner, R. N. Pereira, R. Lechner, K. Klein, H. Wiggers, M. Stutzmann and M. S. Brandt, *Phys. Rev. B,* 2009, **80**, 1–10.

34 H. Zhang, R. Zhang, K. S. Schramke, N. M. Bedford, K. Hunter, U. R. Kortshagen and P. Nordlander, *ACS Phot.*, 2017, **4**, 963–970.

35 S. Zhou, X. Pi, Z. Ni, Y. Ding, Y. Jiang, C. Jin, C. Delerue, D. Yang and T. Nozaki, *ACS Nano*, 2015, **9**, 378–386.

36 X. Pi and C. Delerue, *Phys. Rev. Lett.*, 2013, **111**, 1–5.

37 P. Scherrer, in *Kolloidchemie Ein Lehrbuch*, 1912, pp. 387–409.

38 S. Niesar, A. R. Stegner, R. N. Pereira, M. Hoeb, H. Wiggers, M. S. Brandt and M. Stutzmann, *Appl. Phys. Lett.*, 2010, **96**, 2008–2011.

39 R. N. Pereira, D. J. Rowe, R. J. Anthony and U. Kortshagen, *Phys. Rev. B.*, 2011, **83**, 155327.

40 R. J. Anthony, D. J. Rowe, M. Stein, J. Yang and U. Kortshagen, *Adv. Funct. Mater.*, 2011, **21**, 4042–4046.

41 A. R. Stegner, R. N. Pereira, K. Klein, H. Wiggers, M. S. Brandt and M. Stutzmann, *Phys. B Condens. Matter*, 2007, **401–402**, 541–545.

42 A. Atkinson, *Rev. Mod. Phys.*, 1985, **57**, 437–470.

43 M. P. Hanrahan, E. L. Fought, T. L. Windus, L. M. Wheeler, N. C. Anderson, N. R. Neale and A. J. Rossini, *Chem. Mater.*, 2017, **29**, 10339-10351.

44 Y. Yu, G. Fan, A. Fermi, R. Mazzaro, V. Morandi, P. Ceroni, D.-M. Smilgies and B. A. Korgel, *J. Phys. Chem. C*, 2017, **121**, 23240-23248.

45 D. Jurbergs, E. Rogojina, L. Mangolini and U. Kortshagen, *Appl. Phys. Lett.*, 2006, **88**, 2004–2007.

46 M. Dasog, Z. Yang, S. Regli, T. M. Atkins, A. Faramus, M. P. Singh, E. Muthuswamy, S. M. Kauzlarich, R. D. Tilley and J. G. C. Veinot, *ACS Nano*, 2013, **7**, 2676–2685.

47 M. T. Trinh, R. Limpens and T. Gregorkiewicz, *J. Phys. Chem. C*, , 2013, 117, 5963-5968.

48 M. Govoni, I. Marri and S. Ossicini, *Nat. Phot.*, 2012, **6**, 672–679.

49 D. M. Kroupa, B. K. Hughes, E. M. Miller, D. T. Moore, N. C. Anderson, B. D. Chernomordik, A. J. Nozik and M. C. Beard, *J. Am. Chem. Soc.*, 2017, **139**, 10382–10394.

50 R. Limpens and T. Gregorkiewicz, *J. Appl. Phys.*, 2013, **114**, 074304.

51 S. Miura, T. Nakamura, M. Fujii, M. Inui and S. Hayashi, *Phys. Rev. B*, 2006, **73**, 245333.

52 B. Bruhn, F. Qejvanaj, I. Sychugov and J. Linnros, *J. Phys. Chem. C*, 2014, **118**, 2202–2208.

53 A. L. Efros and M. Rosen, *Phys. Rev. Lett.*, 1997, **78**, 1110–1113.

54 M. C. Beard, K. P. Knutsen, P. Yu, J. M. Luther, Q. Song, W. K. Metzger, R. J. Ellingson and A. J. Nozik, *Nano Lett.*, 2007, **7**, 2506–2512.

55 M. R. Bergren, P. K. B. Palomaki, N. R. Neale, T. E. Furtak and M. C. Beard, *ACS Nano*, 2016, **10**, 2316–2323.

56 E. M. L. D. de Jong, W. D. A. M. de Boer, I. N. Yassievich and T. Gregorkiewicz, *Phys. Rev. B*, 2017, **95**, 195312.

57 L. Mangolini, E. Thimsen and U. Kortshagen, *Nano Lett.*, 2005, **5**, 655–659.

58 R. Limpens, S. L. Luxembourg, A. W. Weeber and T. Gregorkiewicz, *Sci. Rep. 2016,* ***6****, 19566*.

59 K. H. Hartstein, C. S. Erickson, E. Y. Tsui, A. Marchioro and D. R. Gamelin, *ACS Nano*, 2017, **11**, 10430–10438.

60 Y. S. Park, W. K. Bae, J. M. Pietryga and V. I. Klimov, *ACS Nano*, 2014, **8**, 7288–7296.

61 P. P. Jha and P. Guyot-Sionnest, *ACS Nano*, 2009, **3**, 1011–1015.

62 V. I. Klimov, *Annu. Rev. Phys. Chem.*, 2007, **58**, 635–673.

63 I. Robel, R. Gresback, U. Kortshagen, R. D. Schaller and V. I. Klimov, *Phys. Rev. Lett.*, 2009, **102**, 1–4.

64 N. V. Derbenyova and V. A. Burdov, *J. Phys. Chem. C*, 2017, 122, 850-858.

65 L. A. Padilha, W. K. Bae, V. I. Klimov, J. M. Pietryga and R. D. Schaller, *Nano Lett.*, 2013, **13**, 925–932.

66 W. K. Bae, L. A. Padilha, Y. S. Park, H. McDaniel, I. Robel, J. M. Pietryga and V. I. Klimov, *ACS Nano*, 2013, **7**, 3411–3419.